

Cyclostratigraphy and rock-magnetic investigation of the NRM signal in late Miocene palustrine-alluvial deposits of the Librilla section (SE Spain)

Pauline P. Kruiver, Wout Krijgsman, Cor G. Langereis, and Mark J. Dekkers

Paleomagnetic Laboratory Fort Hoofddijk, Utrecht, Netherlands

Received 15 August 2001; revised 21 May 2002; accepted 21 May 2002; published 11 December 2002.

[1] We constructed a high-resolution time frame for the cyclic continental palustrine-alluvial section of Librilla (SE Spain) which covers the onset of the Messinian salinity crisis in the marine realm. The section was dated earlier by *Garcés et al.* [1998], using magnetostratigraphy. We resampled part of the section that contained a reversed overprint in detail to refine the magnetostratigraphy and to investigate the behavior of the natural remanent magnetization (NRM) signal. The detailed sampling yielded a better constrained position of the upper reversal of Chron C3An.1n. By counting the number of cycles in C3An.1n and taking into account the duration of this Chron, we were able to show that the basic sedimentary cycles in Librilla reflect climatic precession. Subsequently, the sedimentary pattern was tuned to the summer insolation curve, providing a high-resolution time. Two intervals of complex NRM behavior were identified, showing normal and reversed overprints. The reversed overprints seemed to be restricted mainly to gray palustrine layers. The analysis of coercivity components revealed no difference between samples with overprints or real NRM directions. We performed fuzzy *c*-means cluster analysis on a geochemical data set to link magnetic behavior to geochemical proxies, resulting in a three-cluster model that roughly describes lithology. Remarkably, all the samples with a normal overprint belong to one particular cluster. The reversed overprints, however, do not show any relation to the cluster partition. We favor the explanation of *Garcés et al.* [1998] that the reversed overprint would be related to the Messinian salinity crisis. **INDEX TERMS:** 1099 Geochemistry: General or miscellaneous; 1520 Geomagnetism and Paleomagnetism: Magnetostratigraphy; 1540 Geomagnetism and Paleomagnetism: Rock and mineral magnetism; **KEYWORDS:** cyclostratigraphy, magnetostratigraphy, isothermal remanent magnetization, fuzzy *c*-means cluster analysis

Citation: Kruiver, P. P., W. Krijgsman, C. G. Langereis, and M. J. Dekkers, Cyclostratigraphy and rock-magnetic investigation of the NRM signal in late Miocene palustrine-alluvial deposits of the Librilla section (SE Spain), *J. Geophys. Res.*, 107(B12), 2334, doi:10.1029/2001JB000945, 2002.

1. Introduction

[2] Sedimentary cycles with periods of ten thousand to a hundred thousand years typically reflect changes in environment caused by climatic oscillations which in turn are controlled by the Earth's orbital cycles. The periods of these orbital cycles allow that a very high-resolution time frame can be obtained from cyclically bedded sequences. For instance, late Miocene and Pliocene Mediterranean marine marl-sapropel sequences are controlled by climatic precession with a period of ~ 22 kyr. The marl-sapropel alternation could be linked to the summer insolation curve [*Hilgen et al.*, 1995; *Lourens et al.*, 1996], which resulted in a time frame with a resolution of better than 10 kyr (half a precession cycle). This permitted dating of paleomagnetic reversals with high accuracy, and the development of an astronomical polarity timescale (APTS). For

the entire Pliocene-Pleistocene and for the late Miocene the APTS has primarily been established on the basis of marine sediments [*Shackleton et al.*, 1990; *Hilgen*, 1991a, 1991b, 1995; *Shackleton et al.*, 1995; *Lourens et al.*, 1996; *Krijgsman et al.*, 1999b]. Also, for continental settings, astronomically controlled variations in sedimentary patterns are now increasingly recognized and better understood. For instance, the early Pliocene lignite-lacustrine marl deposits of Ptolemais (Greece) are clearly related to insolation minima and maxima, respectively [*van Vugt et al.*, 1998], while the Miocene red beds of Armantes (NE Spain) consist of a superposition of small-scale lacustrine/palustrine limestone-red silt layers (precession) and thick limestone beds (eccentricity) [*Krijgsman et al.*, 1997, 1999a]. Additionally, the middle Miocene lacustrine to distal alluvial fan-floodplain deposits from Calatayud basin (NE Spain) show cycles on all orbital scales: from eccentricity (carbonate rich-carbonate poor), obliquity (thick and thin carbonate beds) and precession (carbonate

and clay beds) [Abdul Aziz *et al.*, 2000]. The latter composite section was used to construct an APTS for the late to middle Miocene based on continental sediments [Abdul Aziz, 2001].

[3] Climate changes are recorded by a number of properties. For instance, marine oxygen isotope records reflect the Pleistocene glacial cycles which are driven by orbitally controlled variations in solar radiation [Shackleton and Opdyke, 1973; Hays *et al.*, 1976; Imbrie *et al.*, 1984]. Important climate information on vegetation is contained in pollen records [e.g., Kloosterboer-van Hoeve, 2000], while information on changing faunal habitats on land can be deduced from fossil mammal records [van der Meulen and Daams, 1992; van Dam *et al.*, 2001]. Magnetic properties invariably follow climate fluctuations. An example is the Chinese paleosol-loess sequence, in which the magnetic susceptibility is enhanced in the paleosols during eccentricity maxima after the Mid-Pleistocene transition [Bloemendal *et al.*, 1995; Heller and Evans, 1995]. These sequences provide proxies of, for example, paleoprecipitation [Maher and Thompson, 1999]. Recently, astrochronology has established a link between the marine oxygen isotope records and the continental paleosol-loess sequences [Heller and Liu, 1986; Heslop *et al.*, 2000].

[4] A section that contains both cyclic climate variations and fossil mammals is the Messinian Librilla section in the Neogene Fortuna Basin (south-eastern Spain). Importantly, it contains the interval that includes the onset of the Messinian salinity crisis: the period of most extensive evaporite formation in late Neogene history, triggered by the temporal disconnection of the Mediterranean Basin from the open ocean. First-order time control has already been established by magnetostratigraphy [Garcés *et al.*, 1998]. This earlier study, however, showed that the interpretation of the paleomagnetic signal in Librilla is not always straightforward. A reversed overprint is present in part of the section, seemingly related to lithology.

[5] For the present study, we investigate the paleomagnetic signal in detail, pinpoint the position of the magnetic reversals more precisely, and study the sedimentary cycles. We resampled part of the section spanning Chron C3An.1n, including its upper and lower reversals and made detailed logs of the lithology variations. In this way, we contribute to the assessment of the reliability of the magnetic signal in the alluvial fan/palustrine sedimentary environment. Magnetostratigraphy and cyclostratigraphy are used to construct a time frame. We conclude that the basic gray-red sedimentary cycle is controlled by precession. The natural remanent magnetization (NRM) signal is assessed by rock-magnetic analyses, and by fuzzy *c*-means cluster analysis on geochemical parameters.

2. Geological Setting and Sampling

[6] The Librilla section is situated in the Fortuna Basin and is exposed along the eastern flank of a syncline structure to the north of the village of Librilla (Figure 1). The overall evolution of the Fortuna basin is regarded as the result of a pull-apart basin development, controlled by a NE-SW strike-slip fault system [Garcés *et al.*, 2001]. The Librilla section is grouped into four members, from bottom to top [Garcés *et al.*, 2001]: (1) a cyclic alluvial-palustrine

member (400 m, of which part is shown in Figure 2 and schematically in Figure 8), consisting of alluvial red beds and palustrine organic-rich gray marls, and minor lacustrine limestones. Fossil mammals (zone MN13) indicate a late Turolian (Messinian) age; (2) a prograding conglomeratic member (30 m); (3) a shallow marine member (30 m) of lower Pliocene age, caused by the Pliocene flooding following the Messinian salinity crisis; (4) an upper alluvial member (350 m), consisting of red silts and channelized conglomerates.

[7] Our detailed paleomagnetic resampling scheme was carried out in part of the first member (Figure 2), corresponding to the stratigraphic level from ~235 to 375 m of Garcés *et al.* [2001]. For this part, we made a detailed lithological log for cyclostratigraphic purposes. The section displays a more or less regular alternation between gray palustrine organic-rich reduced facies with abundant gastropod shells and small mammal fossil remains, and pale or bright brown/red alluvial silts with traces of hydromorphous paleosols (Figure 2 and lithological column of Figure 8). Toward the top of the section, the hydromorphous paleosols disappear and are replaced by carbonate crusts (caliche paleosols). Laterally, the hue of the red or brown layers varies.

[8] The lithological variations are cyclic: Thinner dark gray bands, either divided into light-dark-light gray, or dark-light-dark gray (or sometimes in gray-mottled-gray) alternate with thicker red or brown beds which often become mottled toward the contact with the gray bands (see lithological column of Figure 4). In general, the mottling occurs in vertical lines, indicating root traces. We define a basic cycle as one (compound) gray band with one red or brown layer on top of it (Figure 4). In the top of the section there are several bright red, very distinct cycles. The interval below this is much paler, where cycles are not so evident. Below the pale interval, cyclicity is more pronounced again. The alternation of clear and less clear cyclicity suggests that the smaller scale cycles are controlled by precession (period of ~22 kyr), while the bright-pale succession may reflect the eccentricity variation (periods of ~100 kyr and 400 kyr).

[9] We sampled 226 levels over a continuous stratigraphic section of ~120 m, which corresponds to an average sample resolution of ~50 cm (or ~2 kyr, cf. section 5.2). We used a portable, generator-powered drill, which was water-cooled. For each stratigraphic level, four oriented cores were drilled for paleomagnetic, rock-magnetic and geochemical studies. The interval containing samples LCD1 to LCD143 is shown in Figure 2, samples LCD200-LCD283 were taken from a transect below this outcrop.

3. Methods

3.1. Paleomagnetic and Rock-Magnetic Methods

[10] For the determination of the magnetostratigraphy, stepwise thermal demagnetization was applied to at least one sample from each stratigraphic level to isolate ChRM directions. Temperature steps of 50°C were applied up to 450°C, steps of 30°C up to 560°C and steps of 20°C up to 680°C. The samples were heated and cooled in a laboratory-built, shielded furnace with a residual field of less

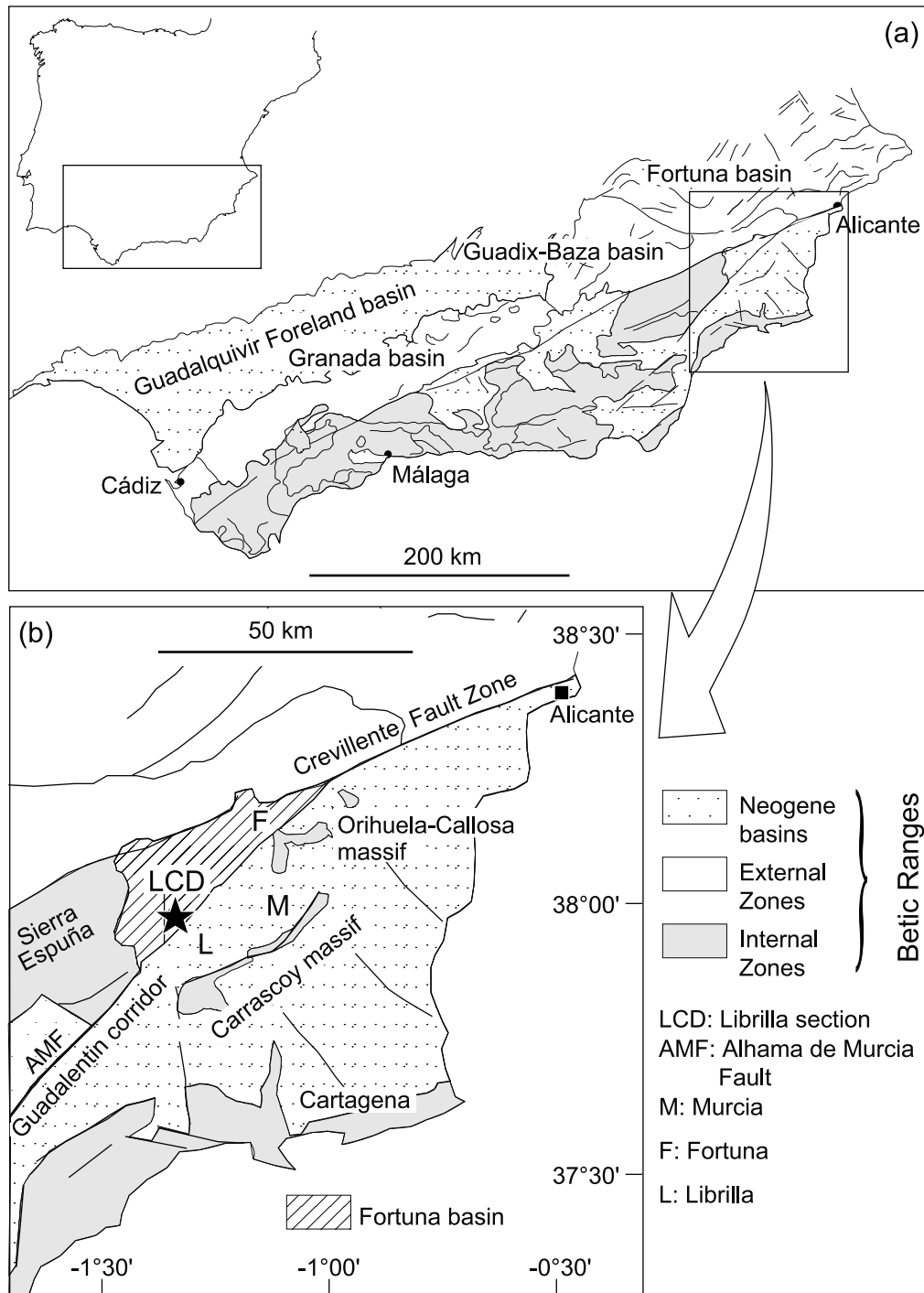


Figure 1. (a) Geological sketch of the Neogene basins in the Betic Ranges. (b) The Fortuna basin (in the eastern Betics) is bounded by two major shear zones: the Alhama de Murcia fault and the Crevillente fault. The section is indicated by an asterisk [after *Garcés et al., 1998*].

than 30 nT. The bulk susceptibility was measured after each heating and cooling step to monitor chemical alterations. When the physical state of a sample did not allow thermal demagnetization, alternating field (AF) demagnetization was applied instead. AF steps were 5–10 mT up to at least 60 mT and in case of suitable demagnetization behavior, further to 80, 120, 200, and 300 mT. A series of 18 samples was treated with a combination of thermal and

AF demagnetization: first, the samples were thermally demagnetized up to 350°C and subsequently AF demagnetization was applied. A double AF demagnetization procedure was employed to screen for gyroremanence [Dankers and Zijderveld, 1981]. The NRM was measured with a horizontal 2G Enterprises SQUID magnetometer (noise level 3×10^{-12} Am²). The directions of the NRM components were determined using principal component

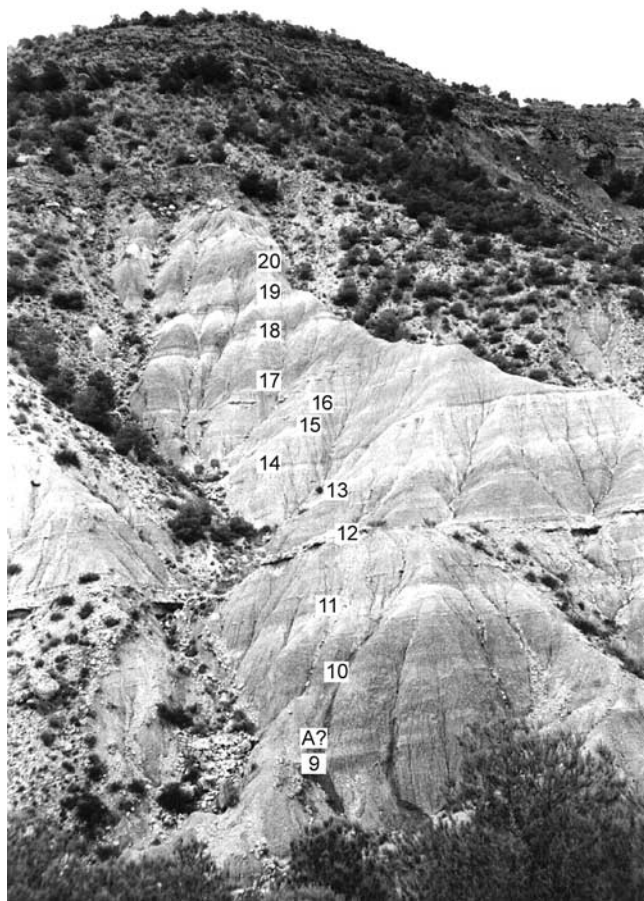


Figure 2. Photograph of the upper 80 m of the section. The numbers correspond to the cycles which are tuned to the summer insolation curve in Figure 12.

analysis including four to six temperature steps or AF steps for each component.

[11] To investigate the reliability of the NRM signal, several rock-magnetic measurements were performed. Thermomagnetic runs were conducted in air for 10 powdered samples from different lithologies up to 700°C on a modified horizontal translation type Curie balance (noise level $5 \times 10^{-9} \text{ Am}^2$) [Mullender *et al.*, 1993]. Acquisition curves of isothermal remanent magnetization (IRM) were determined for 55 stratigraphic levels, using 28–30 acquisition steps with fields up to 2.5T. The peak fields were applied with a PM4 pulse magnetizer and the IRM intensity measured either with a JR5A spinner magnetometer (AGICO, Brno, noise level 10^{-11} Am^2) or with the SQUID magnetometer, depending of the physical state of the samples. The IRM acquisition curves were decomposed into magnetic coercivity components according to the method described by *Kruiver et al.* [2001]. Each coercivity component is characterized by a cumulative lognormal distribution defined by: (1) its saturation IRM (SIRM), (2) the peak field $B_{1/2}$ at which half of the SIRM is reached, and (3) the dispersion DP. Acquisition curves of anhysteretic remanent magnetization (ARM) were measured for 22 levels and treated with the same component analysis as the IRM curves. The maximum applied AF field for ARM acquisition, 300 mT, was reached in 15

approximately equally spaced steps on a logarithmic field scale. The bias field of 31 μT was directed parallel to the AF field.

3.2. Geochemical and Statistical Methods

[12] The concentrations of geochemical elements were determined for all 226 stratigraphic levels with ICP-OES analysis (inductively coupled plasma optical emission spectrometer, Perkin Elmer-type Optima 3000, after total digestion with HF, HNO₃ and HClO₄). Accuracy and precision were checked with laboratory standards and duplicate analyses. The analytical error was better than 5% for Al, Ba, Ca, Fe, K, Mg, Na, and Ti, and better than 10% for the trace elements Cr, Li, Mn, P, Sr and V. Sulfur could not be determined with sufficient reliability, because Ca and Mg peaks interfered with the S peak in the ICP spectrum. The calcium carbonate contents were calculated from the Ca concentrations by assuming that 98% of the Ca resides in CaCO₃. All other elements were subsequently corrected for carbonate contents and will be quoted on a carbonate-free basis (CFB) throughout the paper.

[13] The multivariate fuzzy *c*-means clustering technique [Bezdek *et al.*, 1984] was used to analyze the integral geochemical data set. With this technique, the samples are objectively divided into a user-specified number of internally fairly homogeneous clusters by maximizing the distance between the cluster centers, and minimizing the distance between a sample and its cluster center. Contrary to conventional “hard” cluster techniques, the fuzzy cluster technique does not force a sample into one particular cluster. Instead, it assigns memberships (ranging from 0 to 1) for each sample to each cluster. The weight of each sample to a cluster center is related to this membership coefficient. In this way, intermediate samples have less influence on the position of cluster centers. Moreover, they can be recognized by their similar memberships to more than one cluster. The fuzzy exponent controls the “fuzziness” of the cluster model. A fuzzy exponent of 1 corresponds to hard clustering, while for a fuzzy component approaching positive infinity the clusters completely overlap. Generally, fuzzy exponents of 1.5 to 3 give satisfactory results [Bezdek *et al.*, 1984]. Therefore, we choose a fuzzy component of 1.5. Furthermore, we use the diagonal norm as a measure of distance. Cluster models are run for 2 to 7 clusters. For each specified number of clusters, the cluster partition is determined by iteration [Bezdek *et al.*, 1984]. A random starting partition is chosen for which the cluster centers are calculated. Subsequently, the corresponding membership matrix is determined. The cluster centers and membership matrix are iteratively optimized until a given stopping criterion is reached. Mathematically, the optimal number of clusters corresponds to the model for which the partition parameter F' reaches a maximum and the entropy H' a minimum [Bezdek *et al.*, 1984]. Another method to decide on the optimal number of clusters is displaying the cluster assignments in a nonlinear mapping (NLM) plot [Sammon, 1969]. This is a two-dimensional representation of a multidimensional data cloud, in which the distortion of the distances between cases is kept at a minimum. Clusters that are determined by fuzzy *c*-means clustering should be

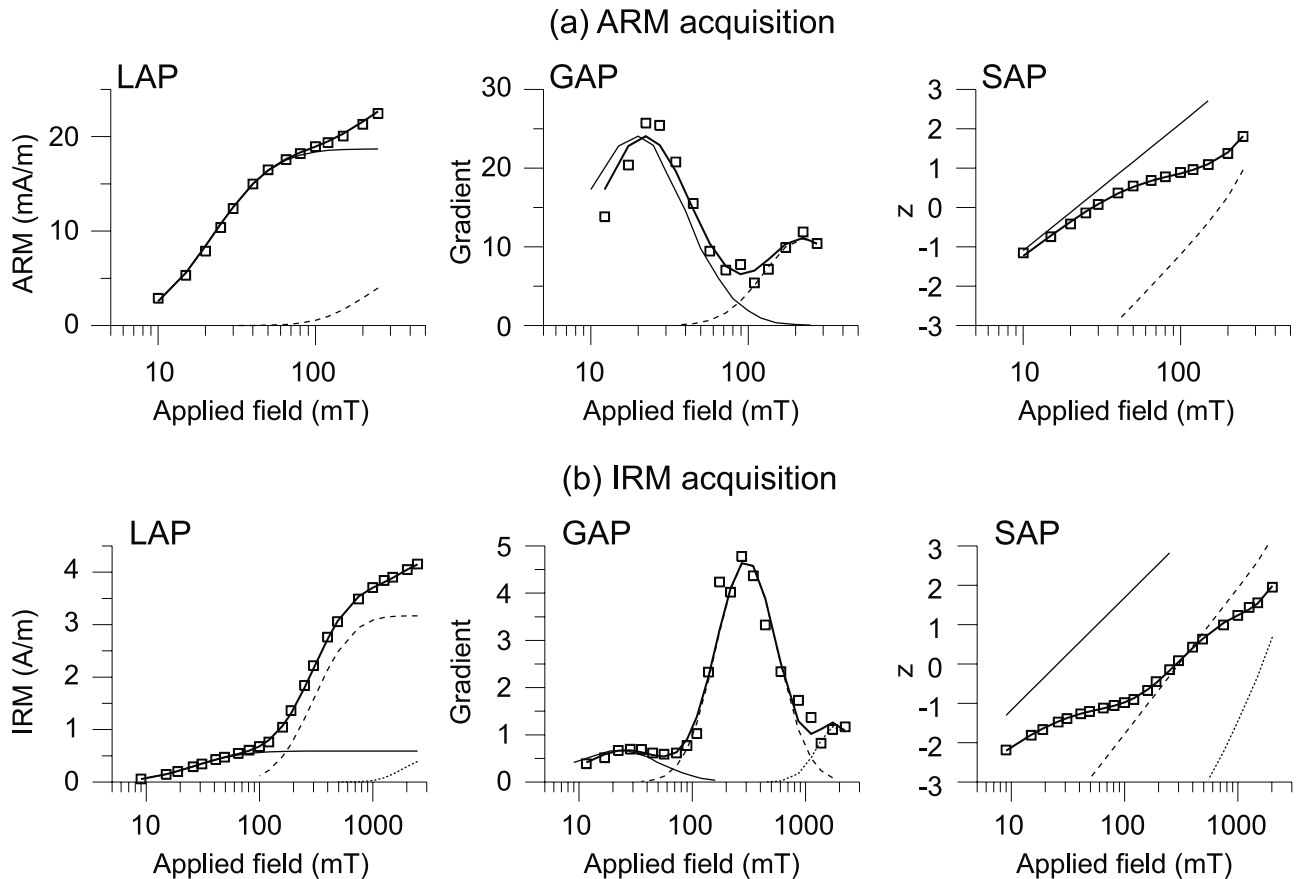


Figure 3. Example of (a) ARM and (b) IRM component analysis for a representative sample (LCD11) from the red lithology of stratigraphic level +6.1 m. Squares represent data points; the thin solid line represents the best fit of component 1, the long dash of component 2, and the short dash of component 3 (IRM only). The thick solid line is the best fit for the sum of the components. From left to right: LAP, linear acquisition plot; GAP, gradient acquisition plot; and SAP, standardized acquisition plot [Kruiver *et al.*, 2001].

well separated in a NLM plot. When the clusters start to blur, the best solution should be sought in a model with fewer clusters.

4. Results

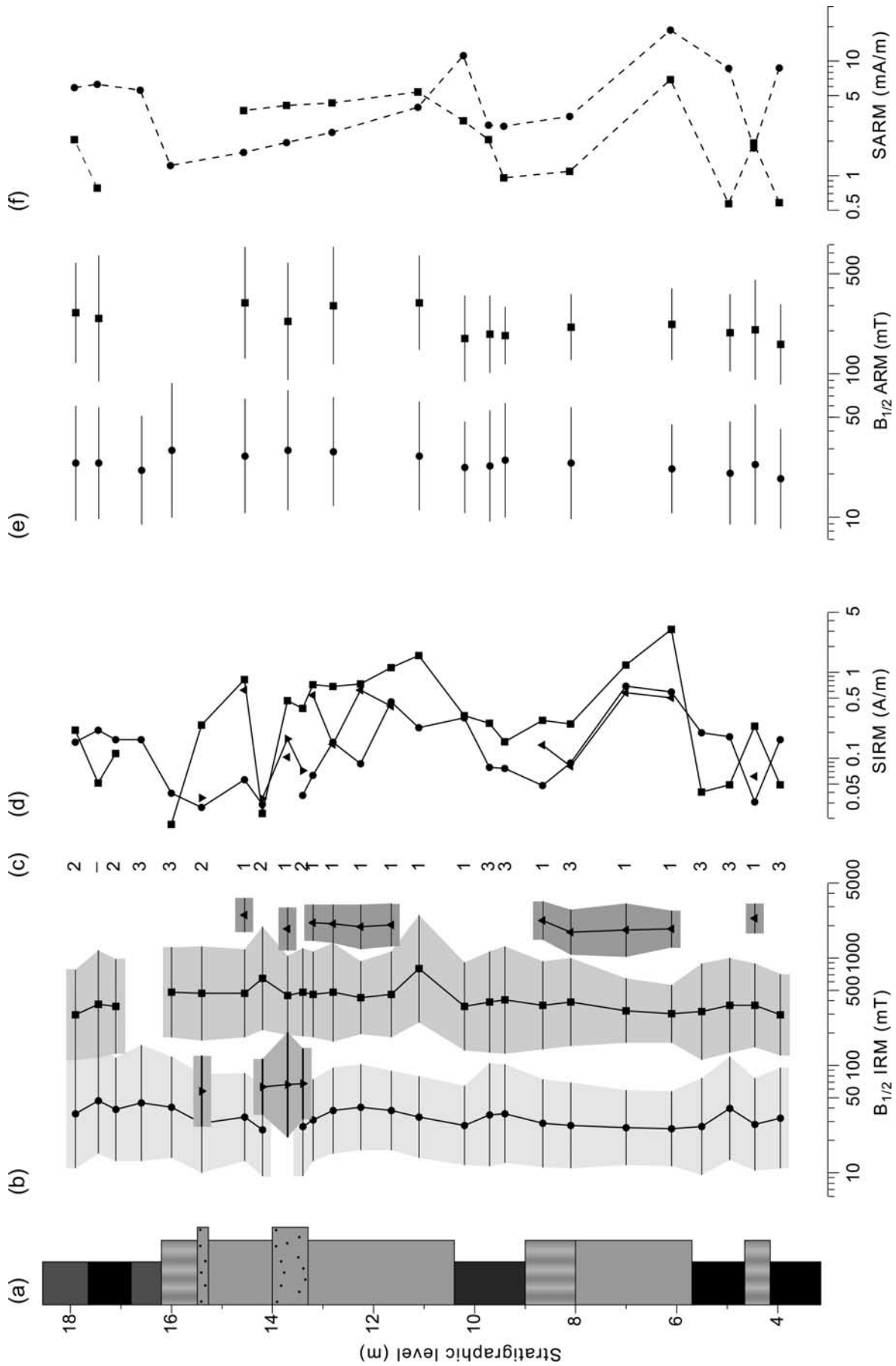
4.1. Rock Magnetism

[14] The thermomagnetic curves $M_s(T)$ of the measured (bulk) samples were so strongly dominated by the paramagnetic matrix that no Curie temperatures could be determined. The cooling curve generally falls below the heating curve, indicating oxidation of a magnetic spinel.

[15] The ARM and IRM component analyses were more successful in characterizing the magnetic mineralogy. The interval ranging from 4 to 18 m was investigated in detail by IRM component analyses, and with slightly less spatial resolution by ARM component analysis. This interval was selected because of its clear cyclicity (Figure 4a).

[16] The ARM and IRM component analyses for a representative sample are shown in Figure 3. In this particular sample, two ARM coercivity components were discriminated and three IRM coercivity components. In general, four coercivity components can be distinguished in the IRM acquisition curves (Figure 4b): two (mutually

exclusive) low-coercivity components, one intermediate-coercivity component and one high-coercivity component. The coercivity component with the lowest coercivity is present in nearly all samples and has a mean $B_{1/2}$ of ~ 34 mT. It is most probably representative of magnetite. The second lowest coercivity component is only present in a few samples in the sandier parts of the red lithology. With an average $B_{1/2}$ coercivity of 63 mT, it might represent oxidized or cation-deficient magnetite, possibly even completely oxidized to maghemite [van Velzen and Zijderveld, 1995; van Velzen and Dekkers, 1999]. The intermediate-coercivity component has $B_{1/2}$ values (average of ~ 400 mT) typical of hematite and generally coexists with the lowest coercivity component. The high-coercivity component can just be detected with the maximum available pulse field of 2.5 T and is therefore not always well constrained. However, the $B_{1/2}$ (~ 2 T) points to goethite. The high-coercivity component is only present in the red lithology, never in the gray marls. Therefore, the presence and absence of the high-coercivity component seem to follow the gray-red cycles. The SIRM values of the low-coercivity and the intermediate-coercivity component seem to follow that of the high-coercivity component (Figure 4d).



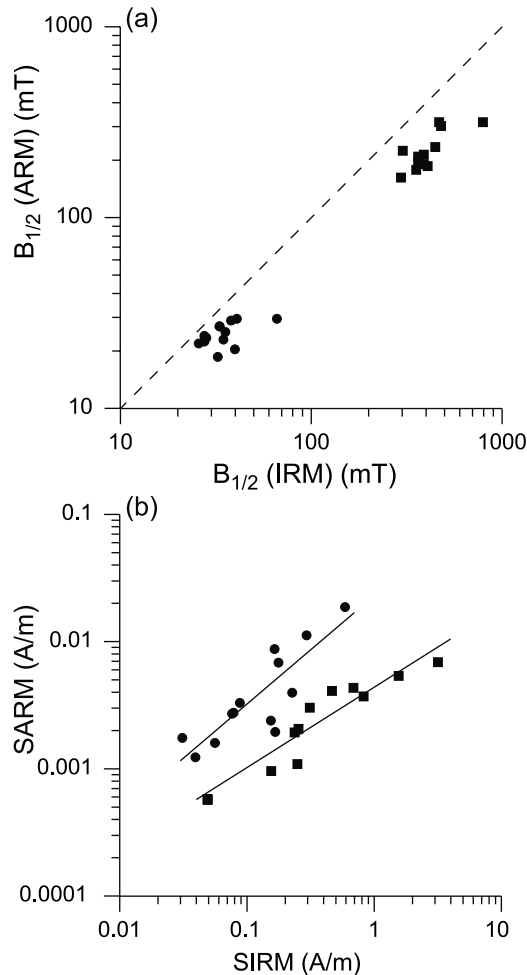


Figure 5. Comparison of ARM and IRM coercivity components. (a) Coercivities. Circles indicate the low-coercivity ARM and IRM components, squares indicate the intermediate-coercivity components. The dashed line represents equal coercivities for ARM and IRM. (b) Saturation ARM and IRM values; symbols as in (a). Regression lines are significant on a 99% level.

[17] The ARM analyses could only detect a maximum of two components, because of its limited field range (maximum of 300 mT) compared to IRM acquisition. In general, the ARM component results are concurrent with the IRM results when the highest IRM coercivity component is not taken into account (Figures 4e and 4f). The patterns of mean coercivity variations are similar, as well as the saturation

patterns. From the similarity between IRM and ARM coercivity patterns, we conclude that the low-coercivity ARM component matches the two low-coercivity IRM components. Correspondingly, the higher coercivity ARM component relates to the intermediate-coercivity IRM component, together referred to as the intermediate-coercivity component.

[18] In Figure 5 we compare the IRM and ARM component parameters. The ARM curves were apparently not sampled with sufficient resolution to distinguish between the two lower coercivity IRM components. Therefore, in the ARM versus IRM comparison the two low-coercivity IRM components are treated as one component. A remarkable observation is that the ARM coercivities are always lower than the IRM coercivities. The differences in coercivities are possibly related to the fact that ARM and IRM are different types of remanences. It should be noted that differences in pulse IRM and static IRM have been reported, where the static IRM displayed a lower coercivity than the pulse IRM [Moskowitz, 1993]. The respective saturation magnetizations show significant power law relationships for both low- and intermediate-coercivity components (Figure 5b). The higher slope of the low-coercivity component probably relates to the fact that ARM preferentially affects spinel phases like magnetite, or might be related to grain size variations.

4.2. Magnetostratigraphy

[19] As the representative thermal demagnetization diagrams in Figure 6 illustrate, the NRM consists of two to three components, described in the following with increasing temperature trajectories. In all samples, a relatively large present-day field component was effectively demagnetized by heating up to 200°C. Although the directions of all samples are scattered, the average direction of the present-day overprint component (no tectonic correction applied) coincides with the expected direction for 38°N (Figure 6f). The intensity of the present-day component, taken as the vector difference between the 90° and 200°C demagnetization steps, is low in the gray layers and higher in the red layers (Figure 8c). A second NRM direction can be defined by either the 250°–480°C or 250°–580°C trajectory, depending on the amount of deterioration of the signal above 480°C. The intensity of this magnetite component displays similar variations as the low-temperature component. Several red samples were unaffected by alteration. In these cases, a partially diverting hematite component could be distinguished at 600°–680°C (e.g., Figures 6a, 6b, 6h, and 6i).

[20] A steep increase in the magnetic susceptibility (measured after each demagnetization step at room temper-

Figure 4. (opposite) (a) Detailed lithological column of two small-scale cycles, corresponding to cycle number 9 and 10 in Figure 2. Black and gray indented blocks represent dark and lighter gray palustrine marls, light gray shadings indicate red alluvial layers, which are dotted in sandier parts. The vertical shading in the top of each red bed represents mottling. (b) Mean coercivities ($B_{1/2}$) for the IRM component analysis. Circles and inverted triangles are low coercivity components, squares represent the intermediate coercivity components and triangles are high coercivity components. The dispersion DP of each component is represented by the horizontal bar and the shaded area. (c) Cluster assignments for the three-cluster model (section 5). (d) SIRM values; symbols as in (b). (e) Mean coercivities for the ARM component analysis. Circles represent the low coercivity ARM component, which corresponds to the low coercivity IRM component; squares indicate the high ARM component, which corresponds to the intermediate IRM coercivity component. DP is indicated by horizontal bars. (f) SARM values; symbols as in (e).

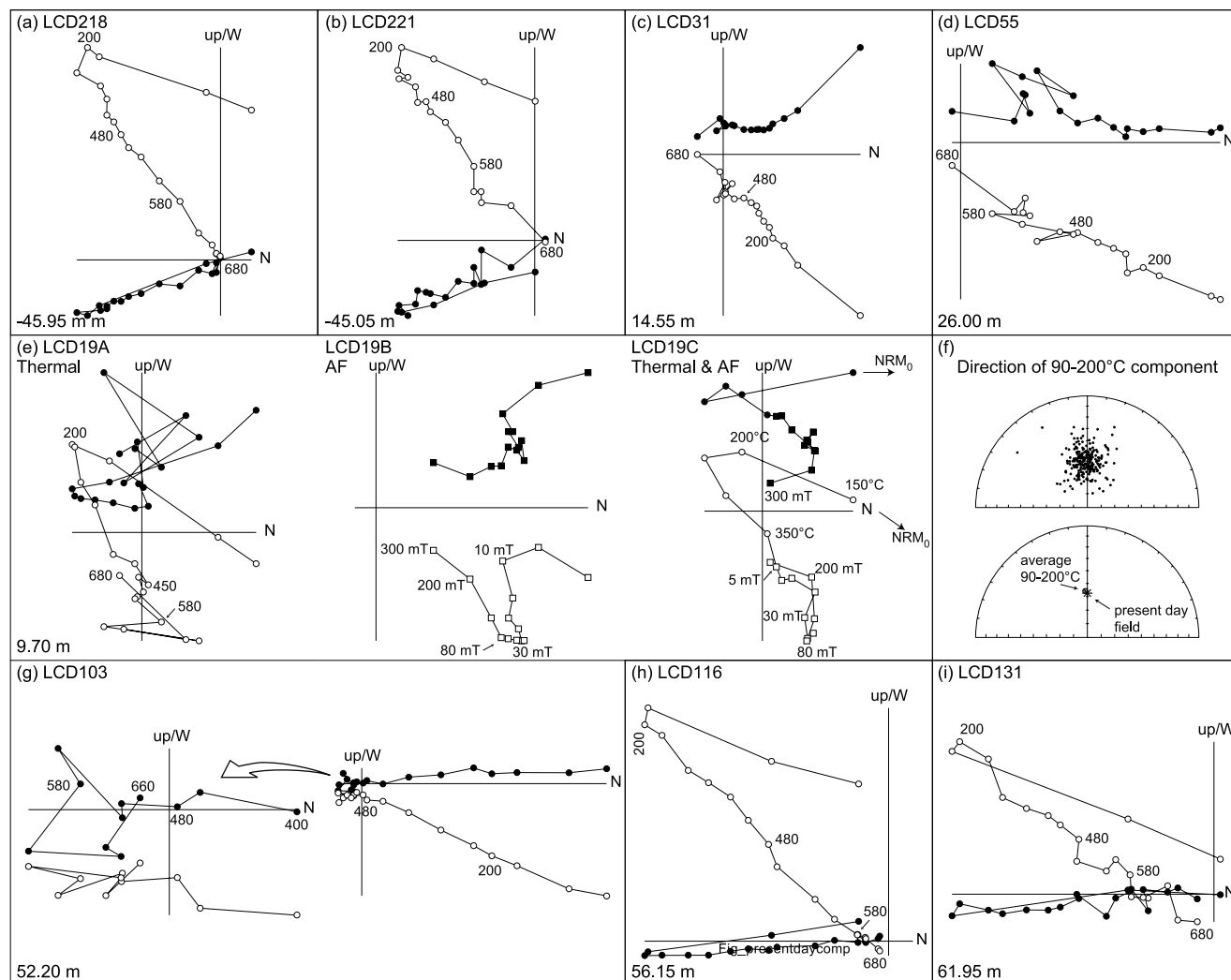


Figure 6. Representative demagnetization diagrams. A comparison between thermal and AF demagnetization, and a combined thermal-AF demagnetization scheme is made for sample LCD19. The high-temperature trajectory for LCD 103 is enlarged. Directions of the 90°–200°C component (no tectonic correction applied) are shown in stereo-projection. For 242 samples, the average declination is 357.5°, the average inclination is 55.8° ($k = 41.7$; $\alpha_{95} = 1.4^\circ$). The geocentric axial dipole (GAD) inclination for the location is 57°, which is very close to that of the 90°–200°C component, thus representing a present-day field overprint.

ature) shows that most samples are altered when heated to temperatures above $\sim 400^\circ\text{C}$ (Figure 7), which might be related to the presence of pyrite in the gray palustrine layers. In the demagnetization diagrams, the trajectories often divert at temperatures above approximately 480°C. They seem to pass the origin at some distance, instead of decaying toward the origin (e.g., Figures 6c and 6d). To determine whether this diverting trajectory is an artifact of progressive heating or represents real directional component, we applied a combination of thermal and AF demagnetization to some samples. For sample LCD19, the thermal and AF trajectories first show a normal present-day overprint. For the temperature steps of 200°–450°C and AF steps of 10–30 mT a reversed component is present (Figure 6e). Temperatures above 480°C do not result in a sensible direction, although a residual normal

direction is suspected. The AF demagnetization, however, clearly demonstrates the presence of a normal component with coercivities characteristic of hematite. Due to the alteration in the thermal experiment, this hematite component could not be resolved. When thermal demagnetization up to 350°C is combined with AF demagnetization (LCD19C), the hematite component can be separated. For most samples, the thermal, AF and thermal-AF results are in agreement. However, the temperature components up to 200°C and up to 480°C have overlapping coercivity spectra. Additionally, the double AF demagnetization procedure duplicates the single run orthogonal AF demagnetization (not shown), indicating that the samples did not suffer from gyroremanence.

[21] The magnetostratigraphy of the resampled section is given in Figure 8b. The interpretation in terms of

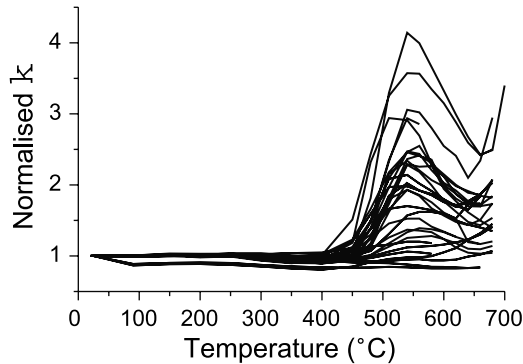


Figure 7. Screening for chemical alteration by monitoring the magnetic susceptibility κ during the thermal demagnetization experiment. κ is measured at room temperature after each heating step, and normalized to the initial value. Initial κ values range from $\sim 40 \times 10^{-6}$ to $\sim 300 \times 10^{-6}$ SI with an average of $\sim 130 \times 10^{-6}$ SI. For temperatures above $\sim 450^\circ\text{C}$ a significant increase in κ occurs, indicating that chemical alteration affects the samples.

polarity zones is not clear-cut. As was detected before by *Garcés et al.* [1998], the normal polarity zone of Chron C3An.1n between -39 and $+33$ m contains many intervals displaying reversed polarities. The quality of most reversed demagnetization diagrams is good, leaving no obvious explanation for their deviating polarity. The only indication that these reversed direction are suspect, is that some of them contain a reversed magnetite and a normal hematite component. They might represent excursions of the geomagnetic field. However, there are no excursions reported in literature for the time interval covered by this section. *Garcés et al.* [1998] interpreted the reversed polarities as overprints, related to the Messinian salinity crisis. The interval of overprints appears to be confined to the interval where the gray palustrine layers are present. The IRM component analysis revealed no clear differences between the reversed overprinted magnetite samples and the normal samples. We adopt the view on cause of the reversed overprints of *Garcés et al.* [1998]: The sea level drop related to the Messinian salinity crisis (during times of reversed polarity) would have caused a temporal lowering of the groundwater table in the near-sea continental environments of the Fortuna basin. This could have induced oxidation of iron sulfides, which are typically present in palustrine/lacustrine sediments, and result in the precipitation of magnetite which acquired a reversed polarity.

[22] The R-N reversal at -39 m coincides with the position given by *Garcés et al.* [1998]. The position of the N-R reversal is improved by the denser sampling scheme. We now place the N-R reversal boundary at $+33$ m, although some normal intervals prevail above this level. However, these samples show very typical behavior, for example, LCD103 in Figure 6. The trajectory up to 480°C heads for the origin, but passes it. For higher temperatures there seems to be a cluster of points to the left of the origin. When this part of the diagram is expanded, however, we observe that there is a structure, although scattered, of a normal component up to approximately 580°C and a

reversed hematite component. Therefore, we hesitate to interpret these samples as representing true normal polarity. The timing of acquisition of the normal component, however, cannot be estimated.

5. Discussion

5.1. Multivariate Geochemical Analysis of the Depositional Environment

[23] The samples were geochemically analyzed to study a possible link between geochemical parameters and magnetic behavior. The elements were corrected for CaCO_3 concentrations and they are always quoted on a carbonate-free basis. In Figure 9, calcium carbonate and several geochemical elements are shown. Generally, the CaCO_3 content varies with lithology: it is elevated in the gray marls. Compound gray palustrine layers often appear as double peaks, for example, at $\sim +16$ and $+18$ m. Elements which more or less mirror the CaCO_3 behavior are Mg, Na, Mn, Sr and P (Figures 6b–6d and Table 1). There is also a positive correlation between Al, Fe, K, Ti, Cr, Li and V (Figures 6e–6g and Table 1). The group of CaCO_3 -correlated elements and the group of the Al-correlated elements show an anti-correlation. Many elements show a noticeable shift in average values near -10 m, from low to higher values for the CaCO_3 -correlated elements. The shift is clearest in the Na record. Also, the Al-correlated elements show a large variability in the interval between $+45$ and $+60$ m.

[24] For the marine environment, the interpretation of various geochemical elements or ratios is reasonably well understood [*Elderfield*, 1990; *Wehausen and Brumsack*, 1999; *Schnetger et al.*, 2000; *Lourens et al.*, 2001]. Fuzzy *c*-means cluster analyses have been applied successfully to marine sediments [*Dekkers et al.*, 1994; *Kruiver et al.*, 1999; *Schmidt et al.*, 1999; *Urbat et al.*, 1999, 2000]. In continental environments, which can be highly variable, the significance of geochemical elements and their ratios is much less clear. The geochemical meaning of the input variables can only be broadly characterized, which limits to a certain extent a complete interpretation of the groupings. Nonetheless, with the success of fuzzy *c*-means cluster analysis in mind, we apply this technique to the Librilla geochemical data set with the hope to find interpretable relationships.

[25] The input parameters included in the fuzzy cluster analysis were: CaCO_3 , Ti/Al, Cr/Al, Mg/Al, Fe/Al, Na/Al, Sr, Mn, V and P (all CFB). Major elements were normalized by Al to create an pseudo-open data set to minimize the closure effect and reduce induced correlations. Trace elements are lognormally distributed and were log-transformed rather than normalized. Generally, Cr and Ti, and to a lesser extent Al, are indicators for detrital input. Ti/Al is in Mediterranean sediments often used to characterize variations in dust input from the Sahara. Because Cr is associated with (ultra)mafic rocks and Ti with acidic rocks, variations in Cr/Al and Ti/Al could indicate differences in provenance area of the sediment. Magnesium and Mg/Al could indicate differences in clay mineralogy and may serve as a proxy for chemical weathering with higher values for Mg/Al indicating less chemical weathering. The Mg content does not show large variations over the

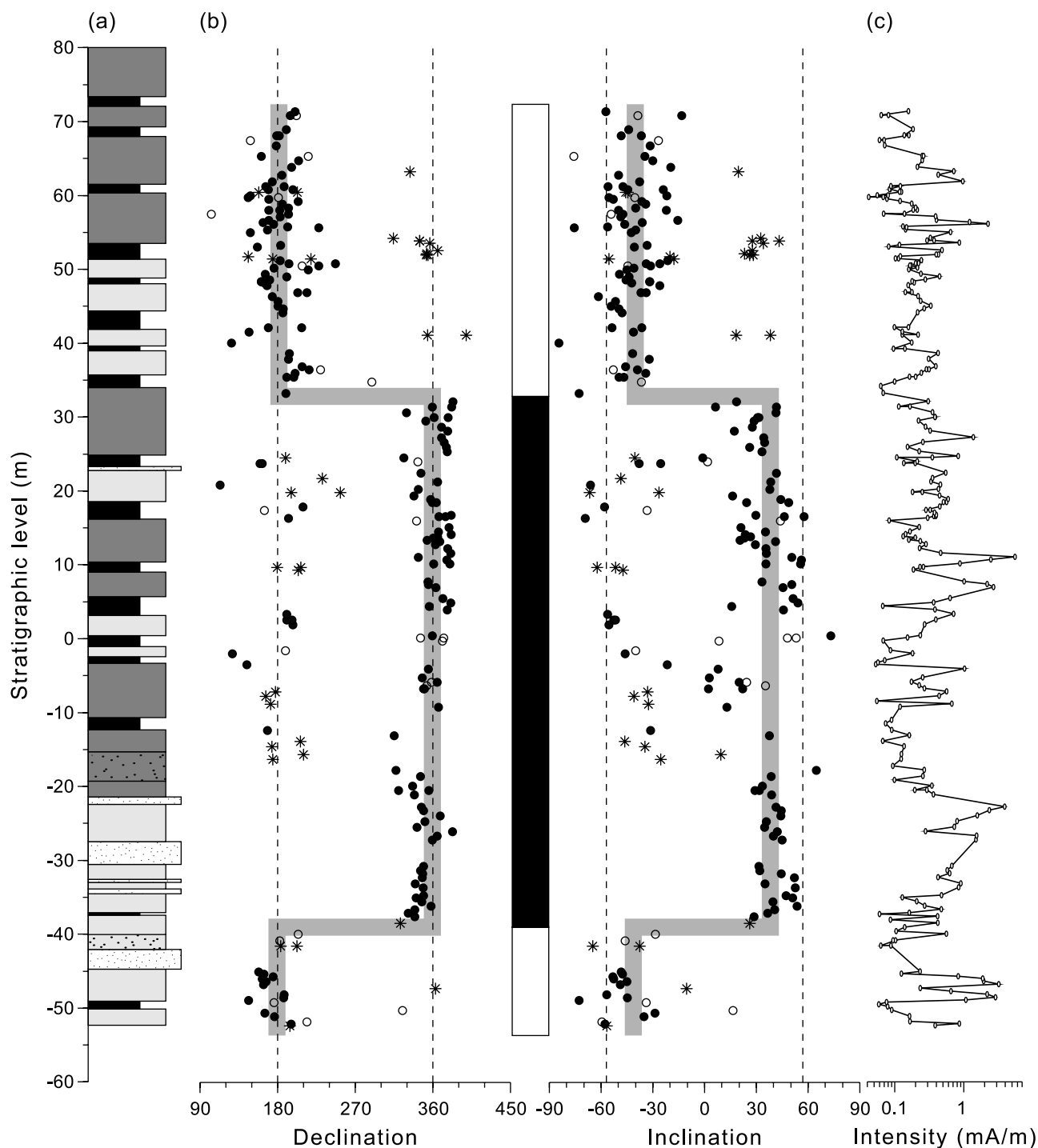


Figure 8. (a) Simplified lithological column. Black indented blocks correspond to (compound) gray palustrine marls. Light shadings correspond to pale red alluvial beds, darker shadings to bright red alluvial beds. Dots indicate sandier layers. (b) Magnetostratigraphy. Solid circles represent ChRM directions (250°–480°C or 250°–580°C) from good quality demagnetization diagrams; open circles represent poor quality data. Stars indicate samples which contained opposite magnetite and hematite directional components, the star indicates the magnetite direction. The dashed vertical lines show the present GAD directions. (c) Intensity of the 90°–200°C component, interpreted as a present-day field overprint.

section suggesting that there were no profound differences in chemical weathering. In marine sediments, raised Fe/Al ratios are taken to indicate diagenetic enrichment of Fe. Again, in marine sediments, Sr is usually isomorphously

substituted in calcium carbonate and is therefore often correlated with CaCO_3 . Also, in the marine environment, Mn and V are found to be sensitive to redox conditions. In oxic sediments, phosphates are sorbed onto iron(oxy)

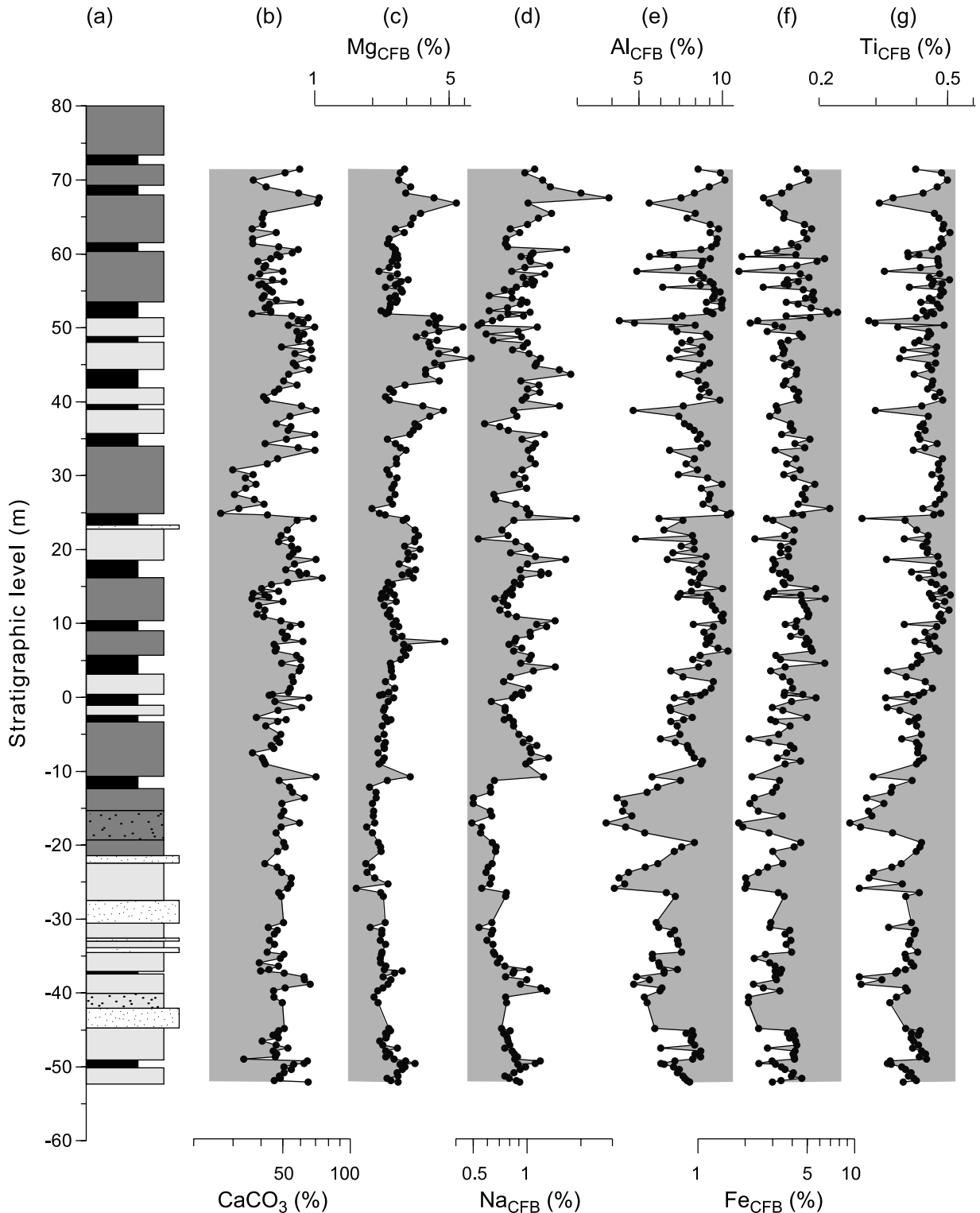


Figure 9. Geochemical elements versus depth. (a) Simplified lithological column (see Figure 8 for explanation). (b) Calcium carbonate. (c) Magnesium. (d) Sodium. (e) Aluminum. (f) Iron. (g) Titanium. Panels c to g are shown on a carbonate-free basis. All ordinates are shown on a logarithmic scale.

(hydr)oxides, and might therefore provide information on redox conditions. The meaning of Na in the continental environment is not well known, but we include Na because it exhibits the clearest shift in values at -10 m. Ratios which primarily relate to source areas are Ti/Al and

Cr/Al. Weathering is covered by the ratio of Mg/Al, and iron enrichment or depletion relative to “average” detrital input is contained in Fe/Al. The correlation matrix of the input parameters is given in Table 2. There is a strong positive correlation between CaCO_3 , $\log(\text{Mn})$ and $\log(\text{Sr})$,

Table 1. Correlation Matrix for the Geochemical Elements on a Carbonate-Free Basis^a

	CaCO ₃	Al	Fe	K	Mg	Na	P	Ti	Cr	Li	Mn	Sr
CaCO ₃												
Al	-0.37											
Fe	-0.40	0.77										
K	-0.31	0.94	0.77									
Mg	0.51											
Na	0.27	0.26			0.30							
P	0.58				0.30	0.45						
Ti	-0.47	0.87	0.62	0.83								
Cr	-0.32	0.92	0.70	0.85				0.77				
Li	-0.25	0.92	0.73	0.91		0.34		0.77	0.81			
Mn	0.67				0.50	0.28	0.36					
Sr	0.64		-0.28			0.52	0.67	-0.40			0.36	

^aAll elements except CaCO₃ are on a carbonate-free basis. Heuristically, absolute values over 0.7 indicate good correlation (bold italics), absolute values between 0.4 and 0.7 indicate moderate correlation (italics). Values of 1 and absolute values below 0.25 are not shown.

and a moderately positive correlation between CaCO₃, Mg/Al and Na/Al. We expect that the cluster analysis will reflect these correlations.

[26] The stability of the cluster solutions was tested by repeating the analysis for a number of different (random) starting conditions and for slightly different input parameter sets by including and excluding various ratios and elements. In all runs, the partition parameter F' had a global maximum and the entropy H' had a global minimum for three clusters. Moreover, for the three-cluster models, the cluster assignments of the samples were nearly identical and thus independent of the variable sets chosen. For higher numbers of clusters samples moved in a seemingly incoherent way between clusters depending on the parameter sets. The three-cluster model thus represents a stable robust solution, and we pursue analyzing this solution for which the NLM plot is shown in Figure 10a.

[27] The cluster centers and the cluster characterizations for the three-cluster model are given in Tables 3 and 4, respectively. The clusters were sorted by CaCO₃ concentration. As expected from the correlation coefficients (Table. 2), the cluster centers of Mg/Al, Na/Al, Mn and Sr show the same variation of low, intermediate and high values for cluster 1, 2 and 3, respectively, as CaCO₃, although the difference in Mg/Al values of the cluster centers of clusters 2 and 3 is relatively small. The basically similar behavior is also expressed in bivariate scatterplots of, for example, CaCO₃ versus Sr (Figure 10b), and

suggests that in the continental environment Sr is isomorphously substituted into CaCO₃, as in the marine environment. In some bivariate scatterplots, the clusters are well separated, whereas in others the clusters (partly) overlap (e.g., Figure 10c). Apparently, in the first case both parameters contribute significantly to the cluster partitioning, while in the second case they are not important for the partitioning.

[28] The three-cluster partition roughly describes lithology variations. For instance, cluster 3 predominates in the gray palustrine samples with higher CaCO₃ contents, and in samples which are very close to the gray layers (Figure 11b). Moreover, the interval from -37 to -12 m in which gray layers are absent, does not contain any cluster 3 samples. Cluster 3 samples seem to be the least chemically weathered, indicated by the highest Mg/Al. Cluster 2 samples are associated with sandier parts of the record. A change in dominant source areas at -10 m seems to be supported the predominance of cluster 2 samples below this level; cluster 2 samples only reappear some 20 m higher. Cluster 1 samples are enriched in iron relative to detrital input (Figure 11c). In the upper 80 m of the section, cluster 1 and cluster 2 seem to follow the bright (1) versus pale (2) red color of the alluvial beds.

5.2. Links Between Geochemical and Rock-Magnetic Parameters

[29] By not including magnetic parameters in the fuzzy cluster analysis, we can investigate the influence of

Table 2. Correlation Matrix for the Ratios of Elements and Elements Used in the Fuzzy *c*-Means Cluster Analysis^a

	CaCO ₃	Fe/Al	Ti/Al	Mg/Al	Cr/Al	Na/Al	log ₁₀ (V)	log ₁₀ (Mn)	log ₁₀ (Sr)	log ₁₀ (P)
CaCO ₃										
Fe/Al										
Ti/Al										
Mg/Al	0.63		0.41							
Cr/Al				-0.42						
Na/Al	0.49			0.42						
log ₁₀ (V)	-0.25	0.34	-0.70	-0.43		-0.31				
log ₁₀ (Mn)	0.76			0.49		0.34				
log ₁₀ (Sr)	0.75			0.29		0.57		0.42		
log ₁₀ (P)	0.58		-0.31			0.37		0.40	0.71	

^aAll elements (except CaCO₃) and ratios are on a carbonate-free basis. Italics as in Table 1.

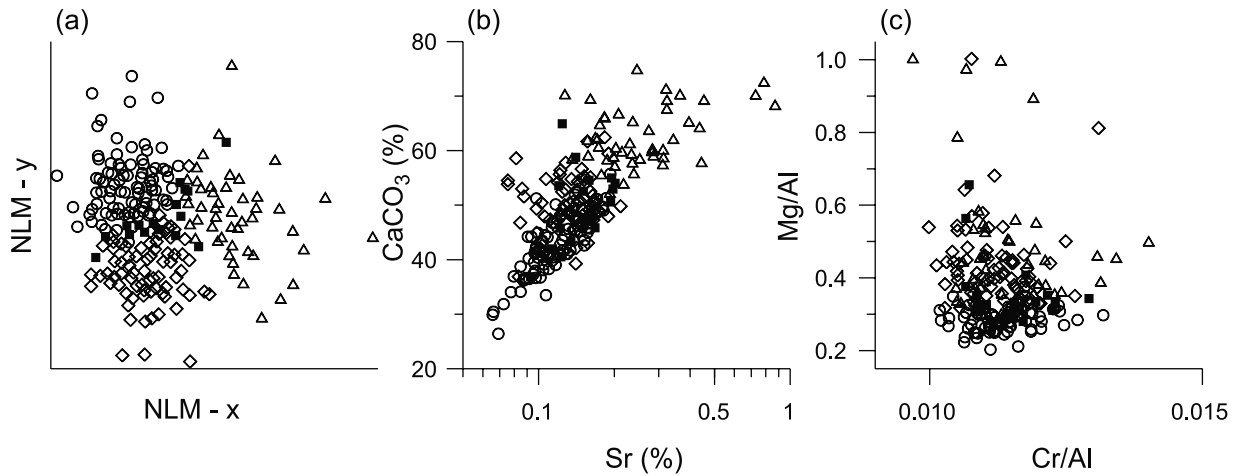


Figure 10. (a) NLM plot of the three-cluster model. Abscissa and ordinate axes have no physical meaning. Cluster 1 samples are represented by open circles, cluster 2 samples by open diamonds, cluster 3 samples by open triangles and samples which are intermediate between clusters by filled squares. Bivariate scatterplots of (b) CaCO_3 versus Sr. (c) Mg/Al versus Cr/Al. Symbols as in (a).

geochemical elements on the magnetic properties by plotting the cluster assignments on the variations of magnetic parameters. In environmental magnetism, the magnetic susceptibility (Figure 11e) is often used as a proxy for climate and this proxy works well in many environments. Examples are the paleosol-loess sequences [Heller and Evans, 1995], lake sediments [see compilation of Dearing, 1999], and deep-sea cores (see compilation of Stoner and Andrews [1999]). However, for this palustrine-alluvial environment the susceptibility does not seem to be logically related to the sedimentary cycles, which are linked to climate (section 5.2). The lithological trends expressed by the clusters are not observed for neither κ_s , nor κ_{CFB} . This limits the straightforward use of susceptibility as a climate proxy in this setting.

[30] Contrary to the susceptibility, the IRM parameters show a relationship with the cluster partition (Figure 4c). The presence of the high-coercivity IRM component interpreted as goethite is confined to cluster 1, the cluster which is enriched in iron. The presence of the second low-coercivity IRM component interpreted as maghemitized magnetite seems to be linked to cluster 2. However, only a few samples with a second low-coercivity IRM component are present in the part of the section which was measured in detail for IRM, and this observation might therefore not be representative for the entire section.

[31] The observed rock magnetic-geochemical links encouraged us to investigate the relationship between demagnetization behavior and (geochemical) clusters. There might be a link between cluster assignments and the temperature up to which the thermal demagnetization yielded sensible directions. The samples for which temperatures up to 480°C could be used seem to be overrepresented in cluster 3: 70% of the samples in this cluster belong to this group. For clusters 1 and 2 $\sim 70\%$ of the samples showed good demagnetization data up to 580°C . The samples which contained normal magnetite and reversed hematite directions appear to be linked to clusters as well. The normal

magnetite directions in the interval of $\sim 40\text{--}65$ m all belong to cluster 1. Not all samples of cluster 1, however, show overprinted directions. The reversed magnetite overprints in the interval of -17 to 23 m do not relate to one particular cluster.

5.3. Cyclostratigraphic Age Model for the Librilla Section and Chron C3An.1n

[32] As described in the geological setting, the section consists of a regular alternation of gray palustrine marls and (pale or bright) red alluvial beds. Spectral analysis of the magnetic susceptibility signal (both as measured and CFB) does not show any clear frequency bands which can be related to the visual cyclicity. Hence, the variability in κ is not a suitable tool for the assignment of the individual sedimentary cycles.

[33] We have defined a basic cycle as one gray marl-red alluvial couplet. The cyclicity is not evident throughout the entire section. The upper ~ 80 m of the section shows clear bright red and less clear pale cycles, while the cyclicity in lower part of the section is much less evident. To estimate the number of cycles in the normal

Table 3. Cluster Centers for the Three-Cluster Model^a

Parameter	Cluster 1	Cluster 2	Cluster 3
CaCO ₃	43.9	49.7	61.2
Fe/Al	0.529	0.484	0.471
Ti/Al	0.0518	0.0607	0.0523
Mg/Al	0.302	0.421	0.456
Cr/Al	0.0113	0.0112	0.0114
Na/Al	0.105	0.129	0.156
V	L	128	94.5
Mn	L	473	502
Sr	L	1196	1356
P	L	0.0976	0.0966
			0.1352

^aAn “L” indicates that parameter values were log-transformed before clustering was applied. All elements (except CaCO₃) are on a carbonate-free basis. Ratios are dimensionless. V, Mn and Sr are in ppm, P is in %.

Table 4. Schematic Representation of the Three-Cluster Model With Characteristic Ratio Values, Their Interpretations and Their Relation to Magnetic Behavior^a

Cluster 1 6	Cluster 2 L	Cluster 3 Δ
Low CaCo ₃ Low Mg/Al High Fe/Al Low Ti/Al	Medium CaCo ₃ Medium-high Mg/Al Low Fe/Al High Ti/Al	High CaCo ₃ High Mg/Al Low Fe/Al Low Ti/Al
dry climate more chemical weathering enriched in iron less dust input (?) or source area different from 2	less chemical weathering depleted in iron more dust input (?) or source area different from 1 and 3	wet, palustrine climate less chemical weathering depleted in iron less dust input (?) or source area different from 2
Related to bright red color (in upper half of the section)	Related to pale red color (in upper half of the section) Related to sandier parts of red layers	Related to gray lithology
<i>Related to high-coercivity IRM component Related to normal magnetite and reversed hematite polarities in interval of -40-65 m</i>		<i>Relative low intensity of 90° - 200°C component</i>

^aRelation to magnetic behavior in italics.

polarity zone between -39 and +33 m, we first assume that the sedimentation rate has been approximately constant [Garcés *et al.*, 2001].

[34] Second, we estimate the average cycle thickness from the part of the section which shows the clearest cyclicity: in the upper 83 m of the section (Figure 2). In this part of the section, 13 to 14 cycles are present. Thus, the average thickness of a sedimentary cycle is 5.9 to 6.4 m. With a constant sedimentation rate, the thickness of sedimentary cycles is not constant, because the duration of the astronomical cycles varies by interference. The normal polarity interval, representing Chron C3An.1n, is 72 m long, and should thus contain 11–12 cycles. Astronomical calibration of Chron C3An.1n showed that it represents 233 kyr in time [Krijgsman *et al.*, 1999b; Steenbrink *et al.*, 2000]. This suggests that the cycles in Librilla have an average periodicity of 19–21 kyr in duration, which is indeed very close to the precession period. Hence, we conclude that the cycles are most probably related to precession-controlled variations in regional climate, and therefore have an orbital origin.

[35] Before we attempt to tune the observed cyclicity to the insolation target curve, we need to establish the phase relationship between the lithologies and the precession or insolation variations. Analyses of X-ray defraction (XRD) and thermographic analyses (TGA) on the clay grain size fraction of eight representative samples from the gray marls and the red beds were inconclusive: the clay content (illite, montmorillonite and kaolinite) and relative concentrations of the clay minerals were rather constant. Therefore, we use the phase relationship established in other continental sections in Spain. We assume that the gray palustrine marls correspond to relatively wet periods during insolation maxima, and the alluvial red beds to relatively dry periods during insolation minima, analogous to the “wet” shallow lake carbonates and “dry” floodplain mudstones of the middle Miocene deposits of Orera [Abdul Aziz, 2001].

[36] The normal polarity zone between -39 and +33 m serves as a starting point for the tuning (Figure 12). The older reversal of C3An.1n is dated astronomically in the Lava section (Greece) at 6.273 ± 0.005 Ma [Steenbrink *et al.*, 2000]. Therefore, the gray marl (cycle 3) just above the reversal is correlated with the insolation maximum at 6.278 Ma. In the top of the section, the four very bright red cycles are correlated to a smaller amplitude, “shouldered” peak (17) and the three large precession maxima above (18, 19 and 20). The gray layers of cycles 16 to 10 are then straightforwardly correlated to the insolation maxima below. The cyclicity is less clear between cycle 10 and cycle 3. The gray marl of cycle 9 is in fact a compound “gray-mottled red-gray” layer, which may well correspond to the double, low amplitude precession maximum at ~ 6.14 Ma. This is supported by the IRM data, which show the presence of the high coercivity component in the mottled red part between the two gray bands, which is characteristic of the red alluvial beds. The dashed correlation lines of cycle 4 and 5 are based on minima in the intensity of the present-day field component (Figure 8c). Moreover, we

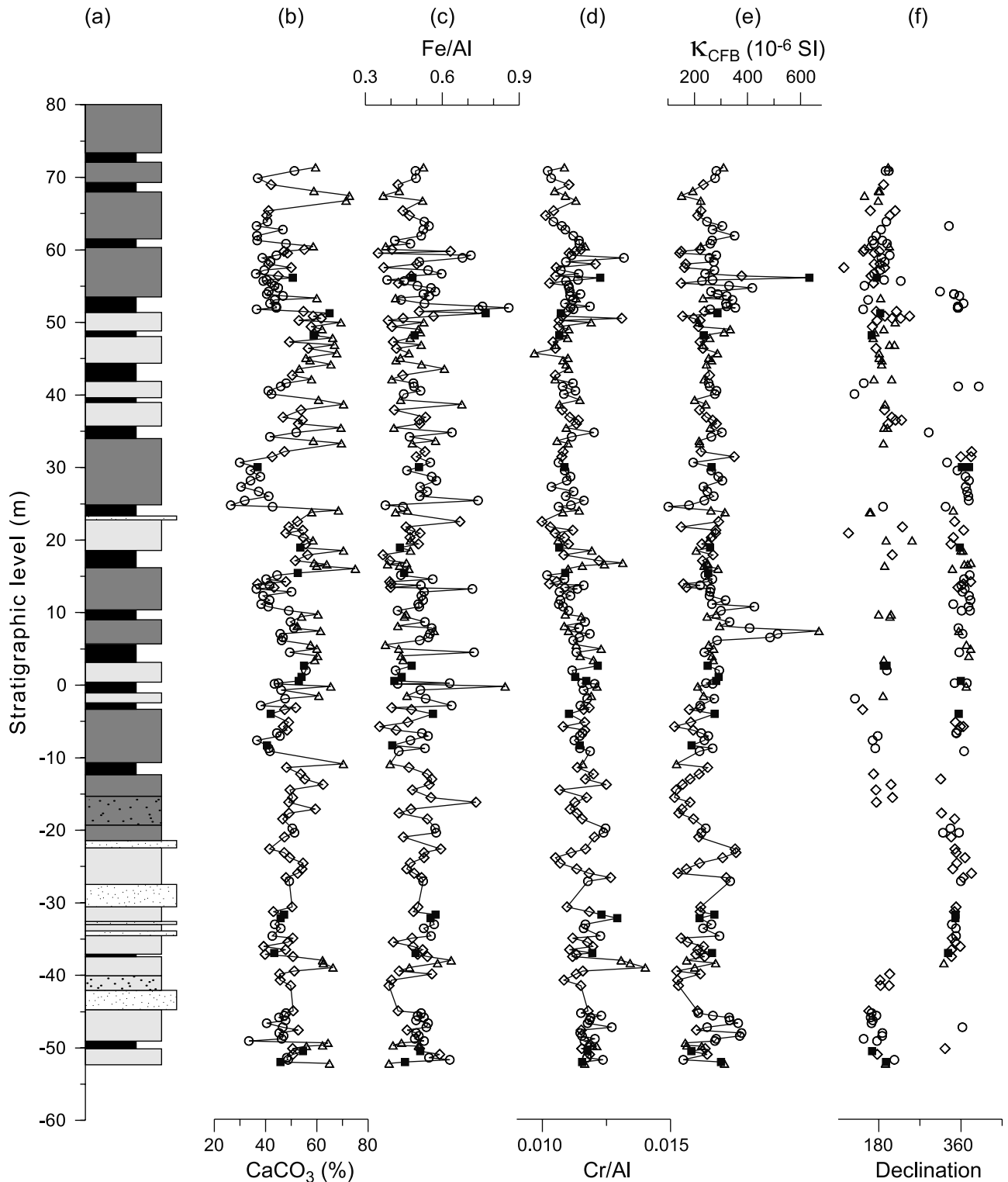


Figure 11. (a) Simplified lithological column (see Figure 8 for explanation). Cluster assignments for: (b) Calcium carbonate. (c) Fe/Al. (d) Cr/Al. (e) κ on a carbonate-free basis (κ of carbonate set to zero). (f) Declination. Symbols as in Figure 10.

would expect 2 to 3 cycles in this interval, based on the sediment thickness.

[37] From the correlation to the insolation curve, it appears that the upper reversal of C3A.1n in Librilla is in agreement

with the APTS [Krijgsman *et al.*, 1999b; Steenbrink *et al.*, 2000] within narrow limits (Figure 12). Additionally, the bright red cycles (cycles 17–20) in the top of the section correspond to the first evaporites of the Messinian salinity

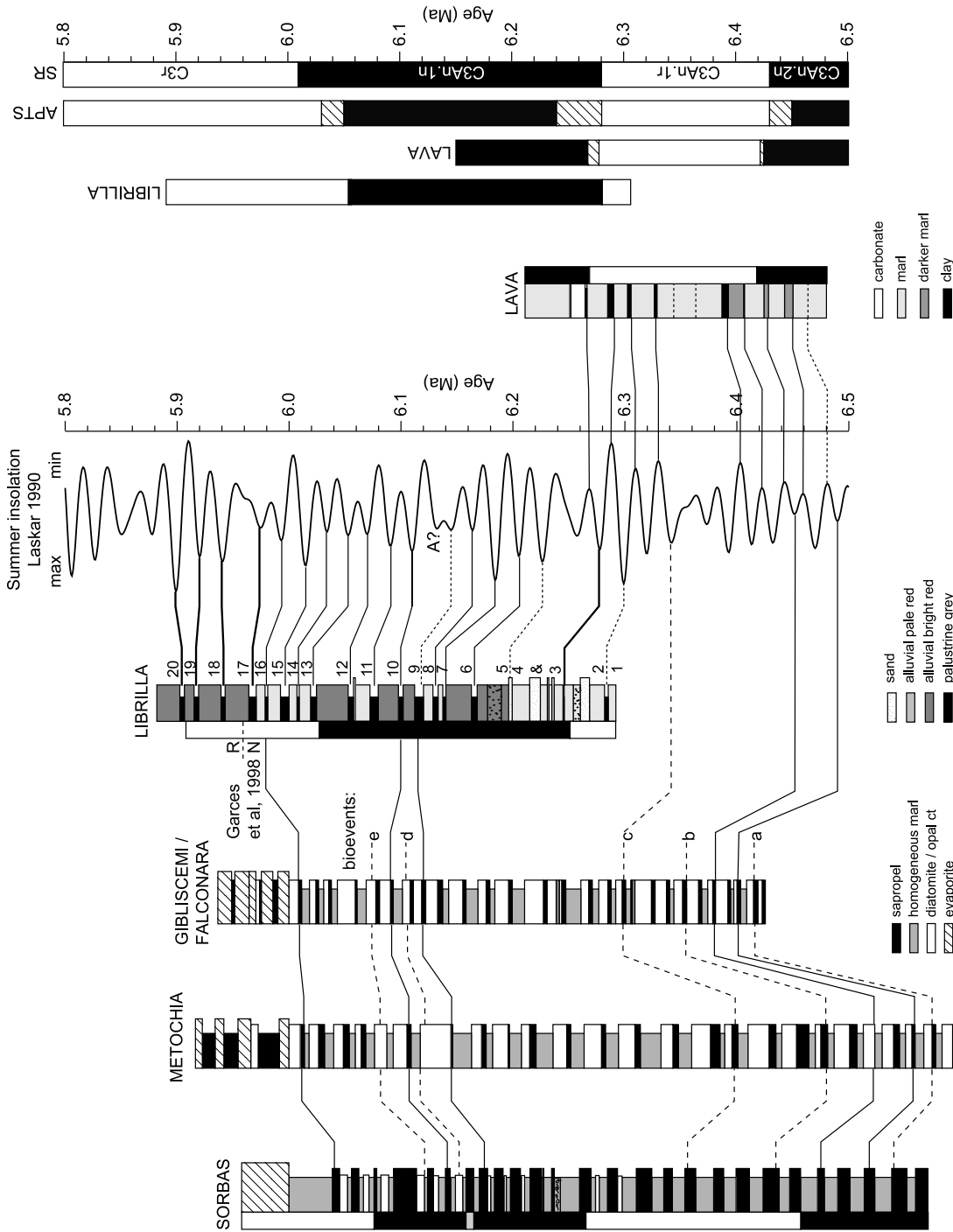


Figure 12. Tuning of the Librilla cycles to the summer insolation and comparison of cycles with other Messinian sections. In the marine sections of Sorbas, Metochia and Gibliscemi [Krijgsman *et al.*, 1999b], sapropel layers are linked to insolation maxima. For the lacustrine marls of Lava [Steenbrink *et al.*, 2000], the clay layers have been linked to insolation minima. For Librilla (this study), the gray palustrine beds with shell fragments are correlated to insolation maxima. Polarity columns compare Chrons C3An.2n through C3r for Librilla, Lava [Steenbrink *et al.*, 2000], the astronomical polarity timescale and Chrons based on constant ocean floor spreading rates [Krijgsman *et al.*, 1999b]. Hatched blocks indicate the error on the reversal boundaries.

crisis in the marine sections of Sorbas (Spain), Metochia (Greece) and Gibliscemi (Sicily, Italy) [Krijgsman *et al.*, 1999b].

6. Conclusions

[38] We studied the sedimentary cycles of the late Miocene section of Librilla in detail, both in the field and by rock-magnetic and geochemical analyses. From the analysis of average cycle thickness, the number of cycles present in Chron C3An.1n, and the astronomically calibrated duration of C3An.1n, we conclude that the gray palustrine-red alluvial cycles in the section of Librilla are linked to climatic precession. The part we investigated in this study covers the age interval of 5.9 to 6.3 Ma, and includes the onset of the Messinian salinity crisis (5.96 Ma [Krijgsman *et al.*, 1999b]). The detailed paleomagnetic sampling has yielded a better definition of the magnetic reversals in the section. However, some intervals in the section show inconsistent polarity behavior. In the upper part of C3An.1n, several samples exhibit reversed polarities. These overprints seem to be related to lithology, they are only present in that part of the section in which the gray layers are well developed. We favor the explanation of Garcés *et al.* [1998] that this reversed overprint is related to the Messinian salinity crisis. In the overlying reversed polarity zone, some isolated levels of samples contained normal polarities residing in magnetite. However, a reversed hematite direction coexists in these samples. Therefore, consistency requires interpreting the normal magnetite directions as overprints.

[39] Fuzzy *c*-means cluster analysis on a set of geochemical data resulted in a statistically robust three-cluster model. The cluster partition roughly describes the main lithological features. The cluster with the highest CaCO₃ concentration predominates in or very close to the gray palustrine marls. Some magnetic properties could be tied to the clusters that were derived with geochemical input parameters only. The cluster with the lowest CaCO₃ content shows a clear relationship with the coercivity components derived from IRM component analysis. A high-coercivity component representing goethite is almost exclusively present in this cluster. Moreover, the presence/absence of the goethite component seems to follow the gray palustrine/red alluvial lithology, respectively. In the top part of the section, all normally overprinted samples belong to the cluster with the lowest CaCO₃ content. Not all samples from this cluster, however, display an overprint. The reversed overprints in C3An.1n are not related to one particular cluster. The fuzzy cluster analysis does thus not provide a clue to distinguish between real and overprinted directions in this interval.

[40] With the improved positions of the reversals, and the demonstration that the sedimentary cycles represent precession it has now become possible to construct a high-resolution time frame (~20 kyr) for the fossil rodents which are present in each palustrine layer in this section. This provides an opportunity for paleontologists to make a detailed environmental reconstruction for the continental realm as a response to changing climate.

[41] **Acknowledgments.** We thank Henk Meijer for measuring part of the IRM and ARM data. Helen de Waard is acknowledged for performing the ICP sample preparations and measurements; Marjan Reith for the TGA and XRD analyses. Many thanks to Miguel Garcés, for his help and company in the field and for the fruitful comments and ideas. This work was funded by the Netherlands Organization for Scientific Research (NWO/ALW) and conducted under the program of the Vening Meinesz Research School of Geodynamics (VMSG).

References

- Abdul Aziz, H., Astronomical forcing in continental sediments. An integrated stratigraphic study of Miocene deposits from the Calatayud-Teruel basin, NE Spain, Ph.D. thesis, Utrecht Univ., Utrecht, 2001.
- Abdul Aziz, H., F. Hilgen, W. Krijgsman, E. Sanz, and J. P. Calvo, Astronomical forcing of sedimentary cycles in the middle to late Miocene continental Calatayud Basin (NE Spain), *Earth Planet. Sci. Lett.*, **177**, 9–22, 2000.
- Bezdek, J. C., R. Ehrlich, and W. Full, FCM: The fuzzy *c*-means clustering algorithm, *Comput. Geosci.*, **10**, 191–203, 1984.
- Bloemendal, J., X. M. Liu, and T. C. Rolph, Correlation of the magnetic susceptibility stratigraphy of Chinese loess and the marine oxygen isotope record: Chronological and palaeoclimatic implications, *Earth Planet. Sci. Lett.*, **131**, 371–380, 1995.
- Dankers, P. H. M., and J. D. A. Zijdeveld, Alternating field demagnetization of rocks, and the problem of gyromagnetic remanence, *Earth Planet. Sci. Lett.*, **53**, 89–92, 1981.
- Dearing, J. A., Holocene environmental change from magnetic proxies in lake sediments, in *Quaternary Climates, Environments and Magnetism*, edited by B. A. Maher and R. Thompson, pp. 231–278, Cambridge Univ. Press, New York, 1999.
- Dekkers, M. J., C. G. Langereis, S. P. Vriend, P. J. M. van Santvoort, and G. J. de Lange, Fuzzy *c*-means cluster analysis of early diagenetic effects on natural remanent magnetisation acquisition in a 1.1 Myr piston core from the Central Mediterranean, *Phys. Earth Planet. Int.*, **85**, 155–171, 1994.
- Elderfield, H., Tracers of ocean paleoproductivity and paleochemistry: An introduction, *Paleoceanography*, **5**, 711–717, 1990.
- Garcés, M., W. Krijgsman, and J. Agustí, Chronology of the late Turolian deposits of the Fortuna basin (SE Spain): Implications for the Messinian evolution of the eastern Betics, *Earth Planet. Sci. Lett.*, **163**, 69–81, 1998.
- Garcés, M., W. Krijgsman, and J. Agustí, Chronostratigraphic framework and evolution of the Fortuna basin (Eastern Betics) since the Late Miocene, *Basin Res.*, **13**, 199–216, 2001.
- Hays, J. D., J. Imbrie, and N. J. Shackleton, Variations in the Earth's orbit: Pacemaker of the ice ages, *Science*, **194**, 1121–1132, 1976.
- Heller, F., and M. E. Evans, Loess magnetism, *Rev. Geophys.*, **33**, 211–240, 1995.
- Heller, F., and T. S. Liu, Palaeoclimatic and sedimentary history from magnetic susceptibility of loess in China, *Geophys. Res. Lett.*, **13**, 1169–1172, 1986.
- Heslop, D., C. G. Langereis, and M. J. Dekkers, A new astronomical time-scale for the loess deposits of Northern China, *Earth Planet. Sci. Lett.*, **184**, 125–139, 2000.
- Hilgen, F. J., Astronomical calibration of Gauss to Matuyama sapropels in the Mediterranean and implication for the Geomagnetic Polarity Time Scale, *Earth Planet. Sci. Lett.*, **104**, 226–244, 1991a.
- Hilgen, F. J., Extension of the astronomically calibrated (polarity) time scale to the Miocene/Pliocene boundary, *Earth Planet. Sci. Lett.*, **107**, 349–368, 1991b.
- Hilgen, F. J., W. Krijgsman, C. G. Langereis, L. J. Lourens, A. Santarelli, and W. J. Zachariasse, Extending the astronomical (polarity) time scale into the Miocene, *Earth Planet. Sci. Lett.*, **136**, 495–510, 1995.
- Imbrie, J., J. D. Hays, D. G. Martinson, A. McIntyre, A. C. Mix, J. J. Morley, N. G. Pisias, W. L. Prell, and N. J. Shackleton, The orbital theory of Pleistocene climate: Support from a revised chronology of the marine d18O record, in *Milankovitch and Climate, Part 1*, edited by A. L. Berger, J. Imbrie, J. Hays, G. Kukla, and B. Saltzman, pp. 269–305, D. Reidel, Norwell, Mass., 1984.
- Kloosterboer-van Hoeve, M. L., Cyclic changes in the late Neogene vegetation of northern Greece. A palynological study, Ph.D. thesis, Utrecht Univ., Utrecht, 2000.
- Krijgsman, W., W. Delahaije, C. G. Langereis, and P. L. de Boer, Cyclicity and NRM acquisition in a continental red bed sequence (Miocene, Spain): Potential for an Astronomical Polarity Time Scale, *Geophys. Res. Lett.*, **24**, 1027–1030, 1997.
- Krijgsman, W., W. Delahaije, C. G. Langereis, and P. L. de Boer, Paleomagnetism and astronomically induced cyclicity of the Armanes section; a Miocene continental red bed sequence in the Calatayud-Daroca basin (Central Spain), *Acta Geol. Hisp.*, **32**, 201–219, 1999a.

- Krijgsman, W., F. J. Hilgen, I. Raffi, F. J. Sierro, and D. S. Wilson, Chronology, causes and progression of the Messinian salinity crisis, *Nature*, 400, 652–655, 1999b.
- Kruiver, P. P., Y. S. Kok, M. J. Dekkers, C. G. Langereis, and C. Laj, A pseudo-Thellier relative palaeointensity record, and rock magnetic and geochemical parameters in relation to climate during the last 276 kyr in the Azores region, *Geophys. J. Int.*, 136, 757–770, 1999.
- Kruiver, P. P., M. J. Dekkers, and D. Heslop, Quantification of magnetic coercivity components by the analysis of acquisition curves of isothermal remanent magnetisation, *Earth Planet. Sci. Lett.*, 189, 269–276, 2001.
- Lourens, L. J., A. Antonarakou, F. J. Hilgen, A. A. M. van Hoof, C. Vergnaud-Grazzini, and W. J. Zachariasse, Evaluation of the Pliocene-Pleistocene astronomical timescale, *Paleoceanography*, 11, 391–413, 1996.
- Lourens, L. J., R. Wehausen, and H.-J. Brumsack, Geological constraints on tidal dissipation and dynamical ellipticity of the Earth over the past three million years, *Nature*, 409, 1029–1033, 2001.
- Maher, B. A., and R. Thompson, Paleomonsoons I: The magnetic record of paleoclimate in the terrestrial loess and palaeosol sequences, in *Quaternary Climates, Environments and Magnetism*, edited by B. A. Maher and R. Thompson, pp. 81–125, Cambridge Univ. Press, New York, 1999.
- Moskowitz, B. M., Rock magnetic criteria for the detection of biogenic magnetite, *Earth Planet. Sci. Lett.*, 120, 283–300, 1993.
- Mullender, T. A. T., A. J. van Velzen, and M. J. Dekkers, Continuous drift correction and separate identification of ferrimagnetic and paramagnetic contributions in thermomagnetic runs, *Geophys. J. Int.*, 114, 663–672, 1993.
- Sammon, J. W., A non-linear mapping for data structure analysis, *IEEE Trans Comput.*, C18, 401–409, 1969.
- Schmidt, A. M., T. Von Dobeneck, and U. Bleil, Magnetic characterization of Holocene sedimentation in the South Atlantic, *Paleoceanography*, 14, 465–481, 1999.
- Schnetger, B., H.-J. Brumsack, H. Schale, J. Hinrichs, and L. Dittert, Geochemical characteristics of deep-sea sediments from the Arabian Sea: A high resolution study, *Deep-Sea Res., Part II*, 47, 2735–2768, 2000.
- Shackleton, N. J., and N. D. Opdyke, Oxygen isotope and paleomagnetic stratigraphy of Pacific core V28-238: Oxygen and isotope temperatures and ice volumes on a 10^5 and 10^6 year scale, *Quat. Res.*, 3, 39–55, 1973.
- Shackleton, N., A. Berger, and W. R. Peltier, An alternative astronomical calibration of the lower Pleistocene timescale based on ODP Site 677, *Trans. R. Soc. Edinburgh: Earth Sci.*, 81, 251–261, 1990.
- Shackleton, N. J., S. Crowhurst, T. Hagelberg, N. G. Pisias, and D. A. Schneider, A new Late Neogene time scale: Application to leg 138 sites, *Proc. Ocean Drill Program: Sci. Results*, 138, 73–97, 1995.
- Steenbrink, J., N. van Vugt, M. L. Kloosterboer-van Hoeve, and F. J. Hilgen, Refinement of the Messinian APTS from sedimentary cycle patterns in the lacustrine Lava section (Servia Basin, NW Greece), *Earth Planet. Sci. Lett.*, 181, 161–173, 2000.
- Stoner, J. S., and J. T. Andrews, The North Atlantic as a Quaternary magnetic archive, in *Quaternary Climates, Environments and Magnetism*, edited by B. A. Maher and R. Thompson, pp. 49–80, Cambridge Univ. Press, New York, 1999.
- Urbat, M., M. J. Dekkers, and S. Vriend, The isolation of diagenetic groups in marine sediments using fuzzy c-means cluster analyses, in *Palaeomagnetism and Diagenesis in Sediments*, edited by D. H. Tarling and P. Turner, pp. 85–94, Geol. Soc., London, 1999.
- Urbat, M., M. J. Dekkers, and K. Krumsiek, Discharge of hydrothermal fluids through sediment at the Escanaba Trough, Gorda Ridge (ODP Leg 169): Assessing the effects on the rock magnetic signal, *Earth Planet. Sci. Lett.*, 176, 481–494, 2000.
- van Dam, J., L. Alcalá, A. Alonso Zarza, J. P. Calvo, M. Garcés, and W. Krijgsman, The Upper Miocene mammal record from the Teruel-Alfambra region (Spain). The MN system and continental Stage/Age concepts discussed, *J. Vert. Paleontol.*, 21, 367–385, 2001.
- van der Meulen, A. J., and R. Daams, Evolution of Early-Middle Miocene rodent faunas in relation to long-term palaeoenvironmental changes, *Palaeogeogr., Palaeoclimatol., Palaeoecol.*, 93, 227–253, 1992.
- van Velzen, A. J., and M. J. Dekkers, Low-temperature oxidation of magnetite in loess-paleosol sequences: A correction of rock magnetic parameters, *Stud. Geophys. Geod.*, 43, 357–375, 1999.
- van Velzen, A. J., and J. D. A. Zijdeveld, Effects of weathering on single-domain magnetite in Early Pliocene marine marls, *Geophys. J. Int.*, 121, 267–278, 1995.
- van Vugt, N., J. Steenbrink, C. G. Langereis, F. J. Hilgen, and J. E. Meulenkamp, Magnetostratigraphy-based astronomical tuning of the early Pliocene lacustrine sediments of Ptolemais (NW Greece) and bed-to-bed correlation with the marine record., *Earth Planet. Sci. Lett.*, 164, 535–551, 1998.
- Wehausen, R., and H.-J. Brumsack, Cyclic variations in the chemical composition of eastern Mediterranean Pliocene sediments: A key for understanding sapropel formation, *Mar. Geol.*, 153, 161–176, 1999.

M. J. Dekkers, W. Krijgsman, P. P. Kruiver, and C. G. Langereis, Paleomagnetic Laboratory Fort Hoofddijk, Budapestaan 17, 3584 CD Utrecht, Netherlands. (kruiver@geo.uu.nl; langer@geo.uu.nl)